From genetic susceptibility to malignant epithelial states: An integrated analysis identifies CLPTM1L and USE1 as key genes in high-grade serous ovarian cancer

ZHENGLIN HE[1,2*], HAI TONG[1,2*], WAN KONG[3*], WEIQIN SU[2*], YUFEI LI[2], GENSHENG WANG[1,2,4], WEN HU[2], LIANG QIAN[2,5] and LUBIN LIU[1,2]

[1]Department of Obstetrics and Gynecology, Chongqing Health Center for Women and Children, Chongqing 401147, P.R. China; [2]Department of Obstetrics and Gynecology, Women and Children's Hospital of Chongqing Medical University, Chongqing 401147, P.R. China; [3]Shanghai Key Laboratory of Regulatory Biology, Institute of Biomedical Sciences and School of Life Sciences, East China Normal University, Shanghai 200241, P.R. China; [4]Department of Obstetrics and Gynecology, Anqing Municipal Hospital, Anqing Medical Center of Anhui Medical University, Anqing, Anhui 246003, P.R. China; [5]Department of Gynecology, Hangzhou Women's Hospital (Hangzhou Maternity and Child Health Care Hospital), Hangzhou, Zhejiang 310008, P.R. China

Received May 21, 2026; Accepted October 1, 2026

DOI: 10.3892/ol.2026.15957

Abstract. High-grade serous ovarian cancer (OC) exhibits marked genetic heterogeneity and diverse epithelial cell states. However, the mechanisms by which genetic susceptibility contributes to these cellular states and tumor phenotypes remain unclear. The present study integrated transcriptome-wide association study (TWAS)/expression quantitative trait locus-based genetic prioritization with single-cell transcriptomic analysis and experimental validation. Genes associated with genetic susceptibility were mapped onto epithelial cells and a composite TWAS activity score was used to classify the cells into three states: High-TWAS state, middle-TWAS state and low-TWAS state. The groups of cells based on these three states exhibited distinct transcriptional programs and intercellular communication patterns. Feature selection using multiple algorithms, together with virtual knockout analysis, further identified cleft lip and palate transmembrane protein 1-like (CLPTM1L) and unconventional soluble N-ethylmaleimide-sensitive factor attachment protein receptor in the endoplasmic reticulum 1 (USE1) as key candidates. Both proteins were expressed at higher levels in SKOV3 and OVCAR3 cells compared with IOSE80 cells. Knockdown of either gene reduced migration, invasion and DNA synthesis in both OC cell lines. CLPTM1L knockdown also reduced fatty acid synthase and activating transcription factor 6 (ATF6) expression, whereas USE1 knockdown reduced mitochondrial fission factor and ATF6 expression. These findings link genetic susceptibility to epithelial cell states and functional tumor phenotypes, and identify CLPTM1L and USE1 as functionally relevant candidate genes in OC.

Correspondence to: Dr Liang Qian or Dr Lubin Liu, Department of Obstetrics and Gynecology, Women and Children's Hospital of Chongqing Medical University, 120 Longshan Road, Chongqing 401147, P.R. China
E-mail: doctorlqian@163.com
E-mail: liulubin1975@126.com

*Contributed equally

Key words: high-grade serous ovarian cancer, genetic prioritization, single-cell RNA sequencing, epithelial state, cleft lip and palate transmembrane protein 1-like, unconventional soluble N-ethylmaleimide-sensitive factor attachment protein receptor in the endoplasmic reticulum 1

Introduction

High-grade serous ovarian cancer (HGSOC) is the most aggressive form of epithelial OC and is characterized by frequent recurrence and treatment resistance (1,2). At the population level, GLOBOCAN 2022 estimated 324,603 new ovarian cancer cases and 206,956 deaths worldwide; 54.9% of new cases occurred in Asia and 21.4% in Europe, illustrating a substantial but geographically heterogeneous global disease burden (3). Most cases of HGSOC are hypothesized to originate from precursor lesions in the distal fallopian tube and subsequently spread at an early stage to the ovary and peritoneal cavity (4). HGSOC also exhibits notable intratumoral heterogeneity. These tumors comprise diverse epithelial, immune and stromal cell populations, and this heterogeneity contributes to variations in disease progression, metastasis and treatment response (5-7). Even within the epithelial compartment, malignant cells can occupy distinct transcriptional states, including inflammatory, stemness-associated and other recurrent state-specific programs described at single-cell resolution (2,5-7). Characterizing these states may help explain the pronounced biological variation among HGSOC tumors.

Inherited genetic susceptibility is an important contributor to HGSOC risk. Genome-wide association studies (GWASs) have identified multiple loci associated with OC risk, including loci specific to HGSOC (8,9). A number of these variants are located in non-coding regions, and thus,

are likely to act by affecting gene regulation rather than by altering protein sequences (9). Transcriptome-wide association studies (TWASs) integrate GWAS data with genetically predicted gene expression to prioritize candidate susceptibility genes (10-12). For example, prior TWAS analyses implicated FZD4 in epithelial OC risk (10) and identified LRRC46 and CHMP4C as candidate HGSOC susceptibility genes, together with a PRC1 splice-associated signal in HGSOC (11). A recent study integrating cis- and trans-expression quantitative trait locus (eQTL) data has further expanded the list of candidate genes linked to OC susceptibility (12). However, these analyses are conducted primarily at the population or tissue level. Although genes associated with inherited risk are identified, it is not revealed where these genes are active within tumors or with which epithelial states they may be associated.

Single-cell RNA sequencing (RNA-seq) has revealed extensive heterogeneity among HGSOC epithelial cells (5-7). In the normal fallopian tube, single-cell RNA-seq has identified secretory, ciliated, transitioning and early-secretory epithelial populations, together with a secretory-to-ciliated differentiation trajectory (13). In HGSOC, malignant epithelial cells exhibit inflammatory and stemness-associated variation (5-7). Other studies have linked tumor cell states involving metabolism/proliferation, cellular defense and DNA-repair programs (2), as well as stress-associated and platinum-resistant malignant populations during treatment evolution (1,14). Variation in epithelial states is also accompanied by changes in ligand-receptor signaling and interactions with surrounding stromal and immune cells (15,16). To the best of our knowledge, the majority of previous studies have focused on transcriptional clustering, differential expression, treatment response or features of the tumor microenvironment. Although GWAS and TWAS studies have used inherited susceptibility as a starting framework to identify HGSOC risk loci and genes (8-12), these risk-prioritized candidates have rarely been mapped onto epithelial states at single-cell resolution. Consequently, it remains unclear whether genes prioritized from inherited risk signals are preferentially active in specific epithelial states and whether they contribute to malignant cellular phenotypes.

In the present study, genetic prioritization was integrated with single-cell transcriptomic analysis to address the aforementioned question. GWAS and eQTL data were first used to identify candidate genes associated with HGSOC. Their activity was then evaluated across epithelial cells, which were classified into high-TWAS state (HTS), middle-TWAS state (MTS) and low-TWAS state (LTS) groups. Transcriptional programs and inferred cell-cell communication were compared among these states. Candidate genes were further prioritized through feature selection using multiple algorithms, external cohort analysis and virtual knockout analysis. Selected genes were subsequently evaluated in OC cell lines using small interfering RNA (siRNA/si) knockdown, migration and invasion assays, 5-ethynyl-2'-deoxyuridine (EdU) analysis, and western blotting. The present study aimed to link inherited susceptibility to epithelial-state heterogeneity and to identify genes that influence OC cell behavior.

Materials and methods

Study design and public datasets. Public data were obtained from the NHGRI-EBI GWAS Catalog (https://www.ebi.ac.uk/gwas/), the Genotype-Tissue Expression (GTEx) Portal (https://gtexportal.org/home/), the NCBI Gene Expression Omnibus (GEO; https://www.ncbi.nlm.nih.gov/geo/) and the NCI Genomic Data Commons (GDC; https://portal.gdc.cancer.gov/). The OC GWAS summary-statistics dataset GCST90244168 originated from the study by Dareng *et al* (9) and was used for genetic prioritization and the regional GWAS/eQTL analyses presented in Figs. 1 and S1. GTEx v8 eQTL data (17) were used to evaluate tissue-specific regulatory support. GSE184880 (6) was the primary single-cell RNA-seq dataset, whereas GSE146026 (5) provided an auxiliary epithelial reference. GSE26712 (18) was used for tumor-vs.-normal expression validation, GSE51373 (19) for platinum-response analyses, and GSE9891 (20), GSE63885 (21) and TCGA-OV (22) for clinical and survival analyses. The processed GSE184880 subset used in the present study comprised five normal samples (GSM5599220-GSM5599224) and three cancer samples (GSM5599225-GSM5599227), totaling 37,024 cells.

Genetic evidence prioritization. Genome-wide significant loci were defined using a threshold of P<5x10-8. For each chromosome, the most significant single-nucleotide polymorphism (SNP) was selected as the lead SNP and a 1-Mb flanking region on either side of the lead SNP was used to define the corresponding risk region. Genetic-prioritization calculations were implemented using custom scripts in Python version 3.13 (Python Software Foundation; https://www.python.org/), with pandas and NumPy used for tabular and numerical processing; no standalone genetic-prioritization software package was used.

GTEx v8 eQTL data were subsequently integrated with the GWAS signals. Ovary, uterus, breast and whole blood were designated as priority tissues. eGenes were filtered according to an eQTL Q<0.05, SNPs located within 1 Mb of the transcription start site and a minor allele frequency (MAF) ≥0.01. Gene-level evidence was evaluated based on consistency in the direction of effect, tissue support and eQTL strength. Genes showing consistent directional evidence in ≥1 tissue or support from ≥2 tissues were retained. Ovary-specific eQTL signals and regional association patterns were further examined for cleft lip and palate transmembrane protein 1-like (CLPTM1L), unconventional soluble N-ethylmaleimide-sensitive factor attachment protein receptor in the endoplasmic reticulum 1 (USE1), multivesicular body subunit 12A (MVB12A) and vacuolar protein sorting 25 homolog (VPS25).

Single-cell RNA-seq analysis. Single-cell preprocessing and downstream analyses were performed in Scanpy version 1.11.4 under Python version 3.13 (https://scanpy.readthedocs.io/). Cells with <200 detected genes or a mitochondrial transcript proportion ≥20% were removed. Genes detected in <3 cells were also excluded. Counts were normalized to 10,000 per cell and then log1p-transformed. Highly variable genes were ranked using the Scanpy highly_variable_genes procedure after normalization and log1p transformation, and the

3,000 genes with the highest resulting variability ranking were retained for downstream analysis.

Principal component analysis was performed, followed by Harmony batch correction using sample identity (harmonypy version 0.0.10; https://github.com/slowkow/harmonypy). A neighborhood graph was constructed using the 15 nearest neighbors and 30 principal components. Leiden clustering was performed at a resolution of 0.6, and uniform manifold approximation and projection (UMAP) visualization was performed using the Python UMAP implementation (umap-learn version 0.5.9.post2; https://umap-learn.readthedocs.io/).

Cell identities were assigned based on module scores derived from canonical markers supported by published HGSOC single-cell studies (5-7): Epithelial cells (EPCAM and KRT8), T cells (CD3D and CD3E), B cells (MS4A1 and CD79A), myeloid cells (CD68 and LYZ), natural killer cells (NKG7 and GNLY), fibroblasts (COL1A1 and DCN), and endothelial cells (PECAM1 and VWF). A total of 3,754 epithelial cells were retained from GSE184880. GSE146026 was processed using a similar workflow and provided an additional epithelial reference comprising 2,207 cells.

TWAS activity scoring and epithelial-state definition. The genetically prioritized gene set was intersected with the genes represented in the single-cell expression matrix. Gene set activity was calculated using area under the curve for cell (AUCell), U-statistic cell scoring (UCell) and single-sample gene set enrichment analysis (ssGSEA)-style rank-based scores were calculated using custom Python 3.13 scripts, whereas AddModuleScore was calculated using Scanpy (https://scanpy.readthedocs.io/). The resulting scores were standardized as Z scores, normalized using min-max scaling and combined into a composite TWAS activity score.

Cells in the upper quartile were classified as HTS, those in the lower quartile as LTS and those in the middle 50% as MTS. This classification yielded 939 HTS, 1,876 MTS and 939 LTS cells.

Differential expression, pathway and cell-cell communication analyses. HTS and LTS cells were used as the primary comparison groups. Differential expression analysis was implemented in custom Python 3.13 scripts and performed using the Mann-Whitney U test. Differentially expressed genes were defined as those meeting both $P<0.01$ and $|\log2 \text{ fold change}|>0.5$; positive log2 fold-change values defined the HTS-associated signature and negative values defined the LTS-associated signature.

Metabolic and signaling pathway activities were summarized using the existing rank-based Python 3.13 pipeline. Spearman's rank correlation was used for continuous score and pathway-activity correlation analyses. Cell-cell communication analysis was implemented with custom Python 3.13 scripts using the precompiled ligand-receptor pair table from the archived analysis. Communication networks were summarized for the cancer samples, and cancer-vs.-normal differences in communication strength and pathway-level patterns were evaluated.

Feature prioritization and virtual knockout analysis. The Random Forest (RF) algorithm was initially used to select the top 50 genes from the candidate set. Eight feature-selection algorithms were subsequently applied: RF, extreme gradient boosting (XGB), gradient boosting machine, extremely randomized trees, recursive feature elimination with RF, adaptive boosting, support vector machine (SVM)-recursive feature elimination and Boruta. The 15 highest-ranking features identified by each method were retained and their strict intersection yielded CLPTM1L, USE1, MVB12A and VPS25. Feature selection and classifier evaluation were implemented in Python version 3.13 using scikit-learn version 1.7.2 (https://scikit-learn.org/), XGBoost version 3.0.3 (https://xgboost.readthedocs.io/) and BorutaPy version 0.4.3 (https://github.com/scikit-learn-contrib/boruta_py).

Classification performance and feature stability were evaluated using five-fold nested cross-validation. The performance of eight classifiers (K-nearest neighbors, linear discriminant analysis, logistic regression, naive Bayes, RF, decision tree, SVM and XGB) was assessed using receiver operating characteristic area under the curve (ROC-AUC), accuracy and F1 score; the F1 score was defined as the harmonic mean of precision and recall. Feature-selection stability was recorded across the outer folds.

The virtual knockout analysis was implemented using custom Python 3.13 scripts with pandas and NumPy. An approximate gene-gene correlation network was constructed using ≤3,000 epithelial cells and the 5,000 genes with the highest expression variance. For each candidate gene, target-gene expression was set to zero and the correlation matrix was recalculated. Network perturbation was quantified from the absolute change in correlation between the target gene and other genes before and after virtual knockout; genes with an absolute correlation change >0.15 were classified as differentially connected genes.

External cohort analyses. The GSE26712 dataset was used to compare candidate gene expression between OC and normal ovarian samples using the Wilcoxon rank-sum test.

The GSE51373 dataset was used to compare CLPTM1L and USE1 expression between platinum-sensitive and platinum-resistant HGSOC samples. When multiple probes mapped to the same gene, the probe with the highest mean expression was retained. ROC analysis was performed to assess the ability of each gene to distinguish between the treatment response groups.

The GSE9891, GSE63885 and TCGA-OV datasets were used to examine associations between gene expression and the available clinical characteristics. Overall survival (OS), progression-free survival (PFS) and disease-free survival (DFS) were analyzed when available. Univariable Cox proportional hazards models were fitted to assess associations between standardized continuous gene expression and time-to-event outcomes.

HTS and LTS bulk signature scores were also calculated using ssGSEA and examined for associations with the available clinical features and survival outcomes.

Cell culture and functional assays

Cell culture. The human OC cell lines SKOV3 and OVCAR3 were purchased from the National Collection of Authenticated Cell Cultures (Shanghai, China) and IOSE80 cells were purchased from Cellverse Bioscience Technology Co., Ltd.

SKOV3 and OVCAR3 cells were cultured in DMEM (Wuhan Servicebio Technology Co., Ltd.) supplemented with 10% fetal bovine serum (Shanghai ExCell Biology, Inc.) and 1% penicillin-streptomycin (Gibco; Thermo Fisher Scientific, Inc.), whereas IOSE80 cells were cultured in RPMI-1640 (Wuhan Servicebio Technology Co., Ltd.) supplemented with 10% fetal bovine serum and 1% penicillin-streptomycin (Gibco; Thermo Fisher Scientific, Inc.). Cells were maintained at 37˚C in a 5% CO_2 atmosphere and used between passages 5 and 20.

Transfection. SKOV3 and OVCAR3 cells were transfected with siRNAs targeting CLPTM1L or USE1 at a final concentration of 50 nM using Lipofectamine® 2000 (Invitrogen; Thermo Fisher Scientific, Inc.) in antibiotic-free medium. Cells were incubated at 37˚C for 48 h, and subsequent experiments were performed 48 h after transfection. A non-targeting negative-control siRNA (si-NC) was included in parallel. Three siRNAs were initially screened for each target gene. si-CLPTM1L-2 and si-USE1-1, which achieved the most efficient knockdown of their respective targets, were selected for subsequent experiments. All siRNAs were synthesized by Beijing Tsingke Biotech Co., Ltd., and their sequences are listed in Table SI.

Reverse transcription-quantitative PCR (RT-qPCR). RT-qPCR was performed to evaluate siRNA-mediated knockdown. Total RNA was extracted from transfected SKOV3 and OVCAR3 cells using Trizol (cat. no. RK30129; ABclonal Biotech Co., Ltd.) and reverse-transcribed using the PrimeScript™ FAST RT Reagent Kit with gDNA Eraser (cat. no. RR092A; Takara Bio, Inc.) according to the manufacturer's instructions. Genomic DNA elimination was performed at 42˚C for 2 min, followed by reverse transcription at 37˚C for 10 min and 85˚C for 5 sec. qPCR was performed using 2X Universal SYBR Green Fast qPCR Mix (cat. no. RK21203; ABclonal Biotech Co., Ltd.). Thermocycling was performed with an initial denaturation at 95˚C for 3 min, followed by 40 cycles of 95˚C for 5 sec and 60˚C for 30 sec, followed by melting-curve analysis. Relative mRNA expression was calculated using the $2^{-\Delta\Delta Cq}$ method (23) with GAPDH as the internal reference. The sequences of forward and reverse primers were as follows: USE1 forward, 5'-GAAGGACAACCAGACCCTGTC-3' and reverse, 5'-GACGCTCTGACTCCGTCTTC-3'; CLPTM1L forward, 5'-TAAGAGCTGGTACTCCTGGT-3' and reverse, 5'-GTCATCAATGAAGGTGTTGA-3'; and GAPDH forward, 5'-CCACCCATGGCAAATTCC-3' and reverse, 5'-TGGGATTTCCATTGATGACAAG-3'.

Migration and invasion assays. Cell migration and invasion were assessed using 24-well Transwell inserts with 8-μm pores. A total of $1x10^5$ cells in 200 μl serum-free medium were seeded into the upper chamber, while 600 μl medium containing 10% FBS was added to the lower chamber. For the migration assay, inserts were used without Matrigel coating; for the invasion assay, the inserts were coated with Matrigel and preincubated at 37˚C for 1 h. Following incubation at 37˚C for 24 h, cells remaining on the upper surface of the membrane were removed, and cells that had migrated or invaded to the lower surface were fixed with 4% paraformaldehyde for 15 min and stained with 0.1% crystal violet for 20 min. Cells were counted in five randomly selected fields under a light microscope.

EdU assay. DNA synthesis was assessed using a red fluorescent EdU assay kit (Beyotime Biotechnology). Cells were incubated with 10 μM EdU at 37˚C for 2 h, fixed with 4% paraformaldehyde for 15 min, and permeabilized with 0.3% Triton X-100 for 10-15 min. The click reaction was performed for 30 min at room temperature in the dark, followed by nuclear staining with Hoechst 33342 for 10 min. EdU-positive cells were visualized by fluorescence microscopy and counted manually; no dedicated image-analysis software was used.

Western blotting. At 48 h after transfection, total protein was extracted from transfected SKOV3 and OVCAR3 cells using RIPA lysis buffer (Beyotime Biotechnology) supplemented with protease inhibitor. Protein concentrations were determined using a BCA assay. Equal amounts of protein (20-30 μg/lane) were separated by 10% SDS-PAGE and transferred to PVDF membranes. The membranes were blocked with 5% non-fat milk for 1 h at room temperature and incubated with primary antibodies overnight at 4˚C. After washing, membranes were incubated with HRP-conjugated goat anti-rabbit IgG H&L secondary antibody (cat. no. HY-P8001; MedChemExpress; 1:5,000-1:10,000) for 1 h at room temperature. Protein bands were visualized using ECL reagent (Beyotime Biotechnology), and densitometric analysis was performed using ImageJ version 1.54u8 (National Institutes of Health). β-actin was used as the loading control. Details of the primary antibodies are provided in Table SII. Based on candidate-specific virtual-knockout outputs, FASN and ATF6 were selected as representative proteins associated with CLPTM1L perturbation, whereas MFF was selected for USE1; ATF6 was additionally examined in both knockdown contexts as a shared stress-related readout. These analyses were exploratory and were not intended to establish direct downstream regulation.

Statistical analysis. Statistical methods were selected according to data type and are specified with the corresponding analyses. The Mann-Whitney U test was used for non-parametric two-group comparisons, and the Kruskal-Wallis test was used for comparisons among multiple clinical groups, as appropriate. Spearman's rank correlation was used to assess associations between continuous variables. Time-to-event outcomes, including OS, PFS and DFS, where available, were evaluated using Cox proportional hazards regression. Computational analyses were performed in Python version 3.13 (Python Software Foundation).

Cell-based quantitative experiments, including RT-qPCR, Transwell assays, EdU assays and western blotting, were each performed in three independent biological replicates, and data are presented as the mean ± SD. Statistical analyses of cell-based experiments were performed using GraphPad Prism version 9.5 (Dotmatics). Comparisons between two independent groups were performed using unpaired two-tailed Student's t-tests. For comparisons among three independent groups, one-way ANOVA followed by Tukey's multiple-comparison post hoc test was used. $P<0.05$ was considered to indicate a statistically significant difference.

Results

Prioritization of candidate genes associated with HGSOC susceptibility based on integrated genetic evidence. OC GWAS signals were integrated with GTEx eQTL data to prioritize

genes associated with HGSOC susceptibility. The candidate genes varied in both the strength of genetic evidence and the breadth of tissue support (Fig. 1A). Among the highest-ranking candidates, CLPTM1L, USE1, MVB12A and VPS25 demonstrated consistent evidence across the genetic prioritization analyses and were retained for further evaluation.

Cross-tissue analyses revealed distinct patterns of regulatory support among CLPTM1L, USE1, MVB12A and VPS25. MVB12A showed the broadest support (36 tissues), followed by USE1 (14 tissues), CLPTM1L (11 tissues) and VPS25 (2 tissues) (Fig. 1B and C).

Ovary-specific eQTL analysis further distinguished the four candidates: The absolute eQTL Z-scores were 5.2 for MVB12A, 3.7 for USE1, 3.7 for VPS25 and 3.3 for CLPTM1L (Fig. 1D). Regional analyses further assessed the relationship between eQTL signals and GWAS risk regions, revealing differences in regional proximity and consistency among the four genes (Fig. S1).

Together, these analyses narrowed the genetically prioritized candidate set to CLPTM1L, USE1, MVB12A and VPS25. These four genes were subsequently evaluated through single-cell state analysis and further candidate selection.

Single-cell transcriptomic analysis defines HTS, MTS and LTS states among HGSOC epithelial cells. Single-cell RNA-seq data from the GSE184880 dataset underwent quality control, dimensionality reduction, clustering and cell type annotation. A total of 37,024 cells were retained, including 3,754 epithelial cells used for the subsequent activity analysis (Fig. S2).

The genetically prioritized gene set was then used to calculate cell-level TWAS activity. Scores generated using AUCell, UCell, ssGSEA and AddModuleScore were combined into a composite activity score. Based on its distribution, the epithelial cells were classified into 939 HTS cells, 1,876 MTS cells and 939 LTS cells (Fig. 2A and C).

UMAP visualization demonstrated the distribution of the three states across the epithelial cell space (Fig. 2A). The composite activity score followed a continuous gradient rather than forming three completely discrete populations. Consistent with the state definitions, HTS cells had the highest composite activity, LTS cells had the lowest composite activity and MTS cells exhibited an intermediate level (Fig. 2A and C). Additional analyses of state dynamics further supported continuity among the three activity states rather than completely independent lineages (Fig. S3).

The distribution of cells derived from cancer and normal samples was then compared. HTS, MTS and LTS cells accounted for 27, 48 and 25% of epithelial cells in cancer samples, respectively, compared with 20, 54 and 26% in normal samples (Fig. 2B and E).

CLPTM1L, USE1, MVB12A and VPS25 also exhibited state-associated expression patterns across HTS, MTS and LTS cells (Fig. 2D). Therefore, their expression was not uniformly distributed across the three activity groups. Together, these findings linked the genetically prioritized candidates to epithelial-state heterogeneity and provided a basis for comparing the biological characteristics of HTS and LTS cells.

HTS and LTS cells exhibit distinct pathway activity and cell-cell communication patterns. To determine whether the activity-based classification captured broader biological differences, pathway activity was compared between HTS and LTS cells. LTS cells showed higher mean activity across the representative pathways, including glycolysis, oxidative phosphorylation and glutathione metabolism (Fig. 3B and C).

Differential expression analysis provided additional evidence of transcriptional differences between HTS and LTS cells (Fig. S3). Thus, the distinction between the two states extended beyond the composite TWAS score and encompassed broader changes in gene expression and pathway activity.

Cell-cell communication was subsequently assessed based on ligand-receptor interactions. Distinct interaction patterns among the major cell types were observed in cancer samples (Fig. 3A), and cancer-vs.-normal changes varied across sender-receiver pairs, including fibroblast-endothelial and myeloid-fibroblast/endothelial interactions (Fig. 3D).

Pathway-level analysis also identified intercellular communication signals with differing relative activities across the analyzed groups (Fig. 3E). Together, the pathway analyses distinguished HTS cells from LTS cells, whereas the communication analysis revealed broader cancer-associated alterations in intercellular signaling.

Integrated analyses prioritize CLPTM1L and USE1 for functional validation. The genetically prioritized candidates were further screened for their ability to distinguish HTS cells from LTS cells. The RF algorithm was initially used to define a common feature pool, followed by feature selection using eight different algorithms. Only four genes were shared across all methods: CLPTM1L, USE1, MVB12A and VPS25 (Figs. 4A and S4).

The stability of this four-gene set was subsequently evaluated using nested cross-validation. XGBoost and Random Forest each achieved an ROC-AUC of 0.977; CLPTM1L and VPS25 were selected in 5/5 outer folds, whereas USE1 and MVB12A were selected in 4/5 folds (Figs. 4D and E, and S5).

The expression levels of the four genes were then evaluated at both the single-cell and bulk transcriptomic levels. Their state-associated expression patterns are shown for all four genes in Fig. 2D. In the external GSE26712 cohort, USE1 and MVB12A exhibited significant expression differences between OC and normal ovarian samples (Fig. 4B).

Additional treatment-response and clinical analyses of CLPTM1L and USE1 evaluated platinum and first-line treatment response, survival and available clinical characteristics across GSE51373, GSE63885, GSE9891 and TCGA-OV (Fig. S6). Clinical evaluation of HTS- and LTS-associated bulk signatures, including cohort coverage, treatment-response discrimination and survival associations, is presented in Fig. S7.

Virtual knockout analysis was subsequently performed to assess how perturbation of the four candidates affected epithelial cell correlation networks. CLPTM1L produced the strongest overall perturbation; VPS25 also produced evident network alterations, of a magnitude similar to USE1 (mean $|\Delta\text{correlation}|$, $2.71\text{x}10^{-5}$ vs. $2.80\text{x}10^{-5}$, respectively) (Fig. 4C). Additional candidate-specific network changes are presented in Fig. S8.

Because the experimental scope was limited to two representative genes, CLPTM1L was selected on the basis of the strongest virtual-knockout perturbation, whereas USE1 combined

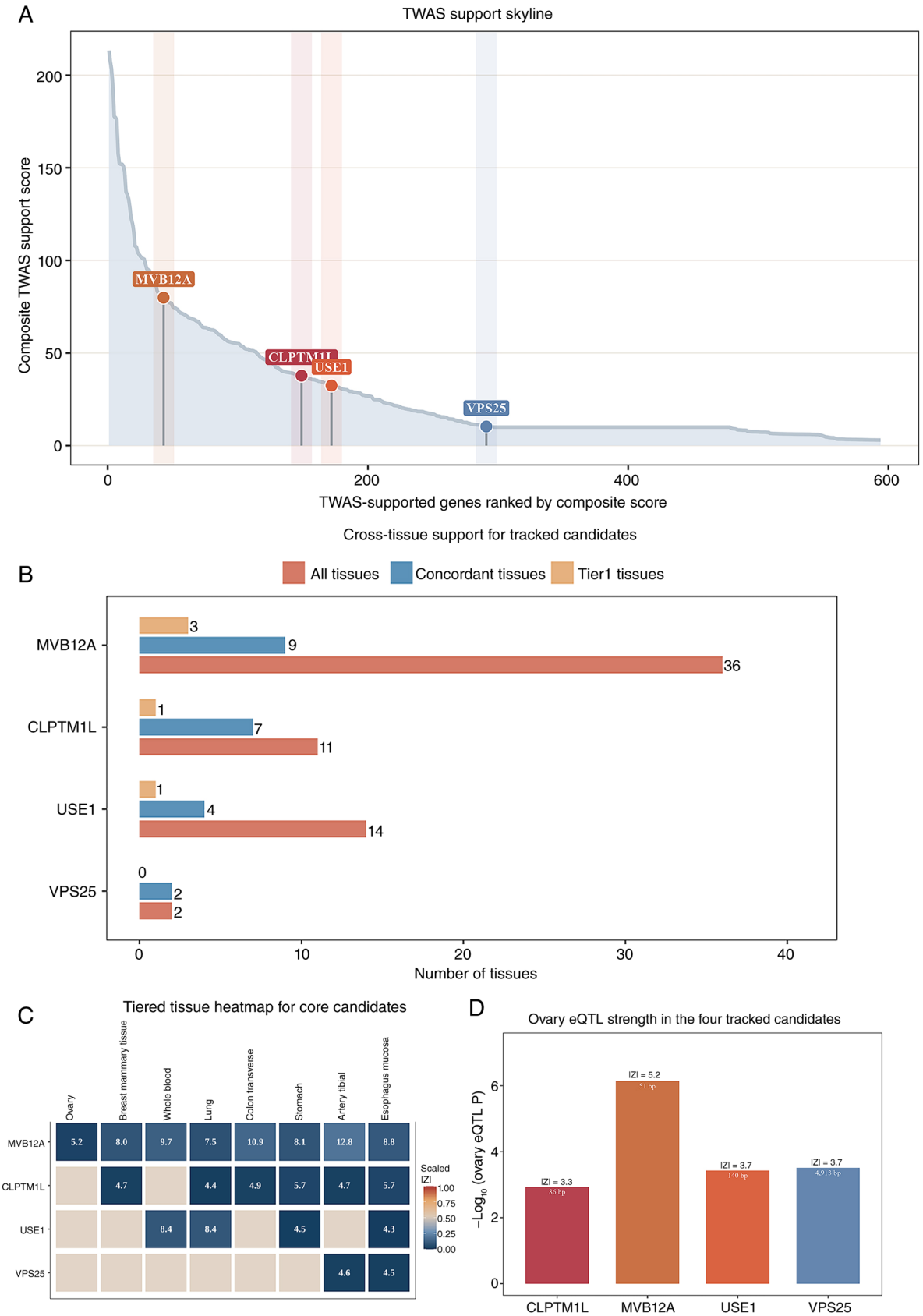


Figure 1. Integrated genetic evidence prioritizes candidate genes associated with high-grade serous ovarian cancer susceptibility. (A) Skyline plot of TWAS support showing candidate genes ranked according to the composite genetic-support score, with MVB12A, CLPTM1L, USE1 and VPS25 highlighted. (B) Cross-tissue support for the four selected candidates. The bars indicate the total number of supporting tissues, the number of tissues with concordant evidence and the number of tier 1 tissues. (C) Tiered tissue heatmap showing the relative eQTL support for MVB12A, CLPTM1L, USE1 and VPS25 across representative tissues. (D) Ovary-specific eQTL strength for CLPTM1L, MVB12A, USE1 and VPS25. Numbers above the bars indicate the absolute eQTL Z-score and the distance to the nearest genome-wide association studies signal. TWAS, transcriptome-wide association study; MVB12A, multivesicular body subunit 12A; CLPTM1L, cleft lip and palate transmembrane protein 1-like; USE1, unconventional soluble N-ethylmaleimide-sensitive factor attachment protein receptor in the endoplasmic reticulum 1; VPS25, vacuolar protein sorting 25 homolog; eQTL, expression quantitative trait locus.

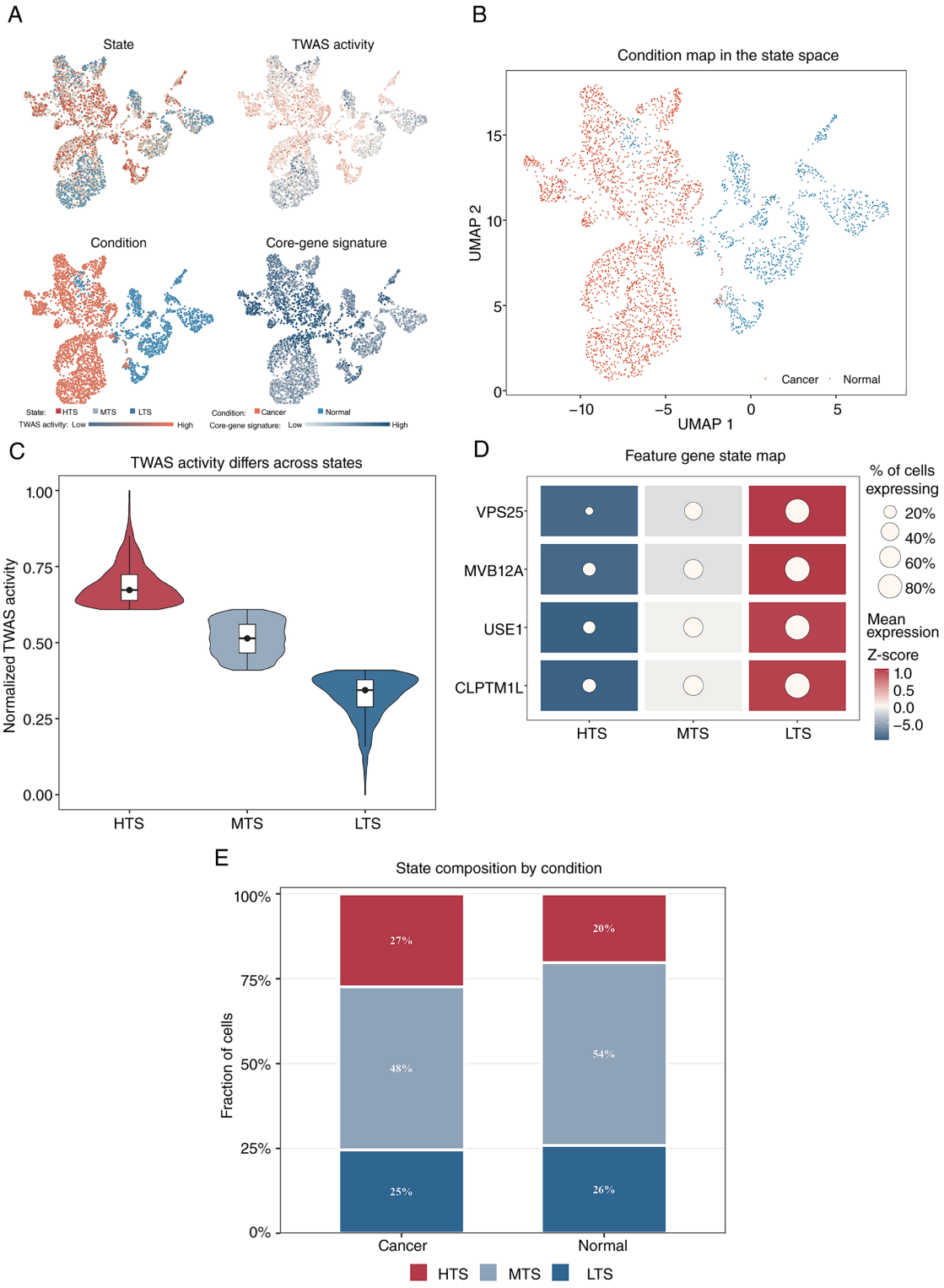


Figure 2. Single-cell transcriptomics analysis defines HTS, MTS and LTS cells among high-grade serous ovarian cancer epithelial cells. (A) UMAP plots of epithelial cells colored by TWAS activity state, composite TWAS activity, sample condition and core-gene signature. (B) Distribution of epithelial cells derived from cancer and normal samples in UMAP space. (C) Violin plots showing normalized TWAS activity across HTS, MTS and LTS groups. (D) State-associated expression levels of CLPTM1L, USE1, MVB12A and VPS25. Dot size indicates the percentage of cells expressing each gene and color indicates the mean expression Z-score. (E) Relative proportions of HTS, MTS and LTS cells in cancer and normal samples. HTS, n=939; MTS, n=1,876; and LTS, n=939. HTS, high-TWAS state; MTS, middle-TWAS state; LTS, low-TWAS state; UMAP, uniform manifold approximation and projection; TWAS, transcriptome-wide association study; CLPTM1L, cleft lip and palate transmembrane protein 1-like; USE1, unconventional soluble N-ethylmaleimide-sensitive factor attachment protein receptor in the endoplasmic reticulum 1; MVB12A, multivesicular body subunit 12A; VPS25, vacuolar protein sorting 25 homolog.

significant external expression support in GSE26712 with substantial network perturbation. MVB12A showed external expression support but weaker network perturbation, whereas VPS25 showed evident network alteration but no significant external expression difference in GSE26712. MVB12A and VPS25 therefore remain candidates for future functional evaluation.

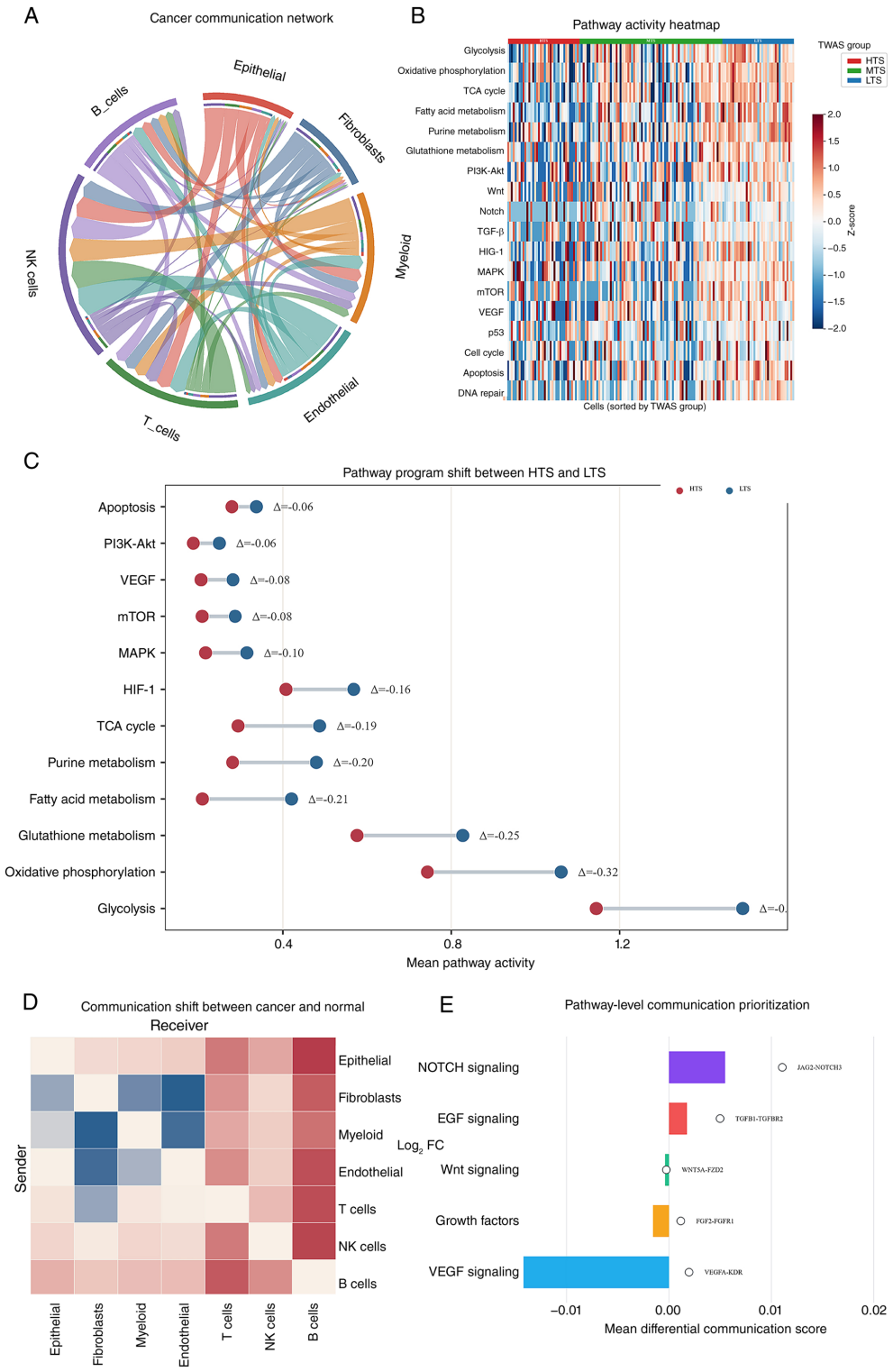


Figure 3. HTS and LTS cells exhibit distinct pathway activity and cell-cell communication profiles. (A) Inferred cell-cell communication network in cancer samples showing interactions among epithelial cells, fibroblasts, myeloid cells, endothelial cells, T cells, NK cells and B cells. (B) Heatmap of representative metabolic and signaling pathway activities across epithelial cells ordered by TWAS activity state. (C) Comparison of mean pathway activities between HTS and LTS groups. Paired points represent the two states, with red circles indicating HTS and blue circles indicating LTS, and Δ denotes the difference in mean activity between HTS and LTS groups. (D) Heatmap showing cancer-vs.-normal changes in inferred communication strength across sender-receiver cell type pairs. Values are presented as $\log_2$ FC. (E) Pathway-level communication summary showing differential communication scores for selected signaling pathways. Labeled circles indicate representative ligand-receptor pairs. TWAS, transcriptome-wide association study; HTS, high-TWAS state; MTS, middle-TWAS state; LTS, low-TWAS state; NK, natural killer; FC, fold change; TCA, tricarboxylic acid; HIF-1, hypoxia-inducible factor-1.

CLPTM1L knockdown inhibits OC cell migration, invasion and DNA synthesis, and is accompanied by reduced FASN and ATF6 expression. Baseline western blotting demonstrated higher CLPTM1L protein expression in SKOV3 and OVCAR3 OC cells than in IOSE80 cells (Fig. 5A and B). siRNAs were then screened for their

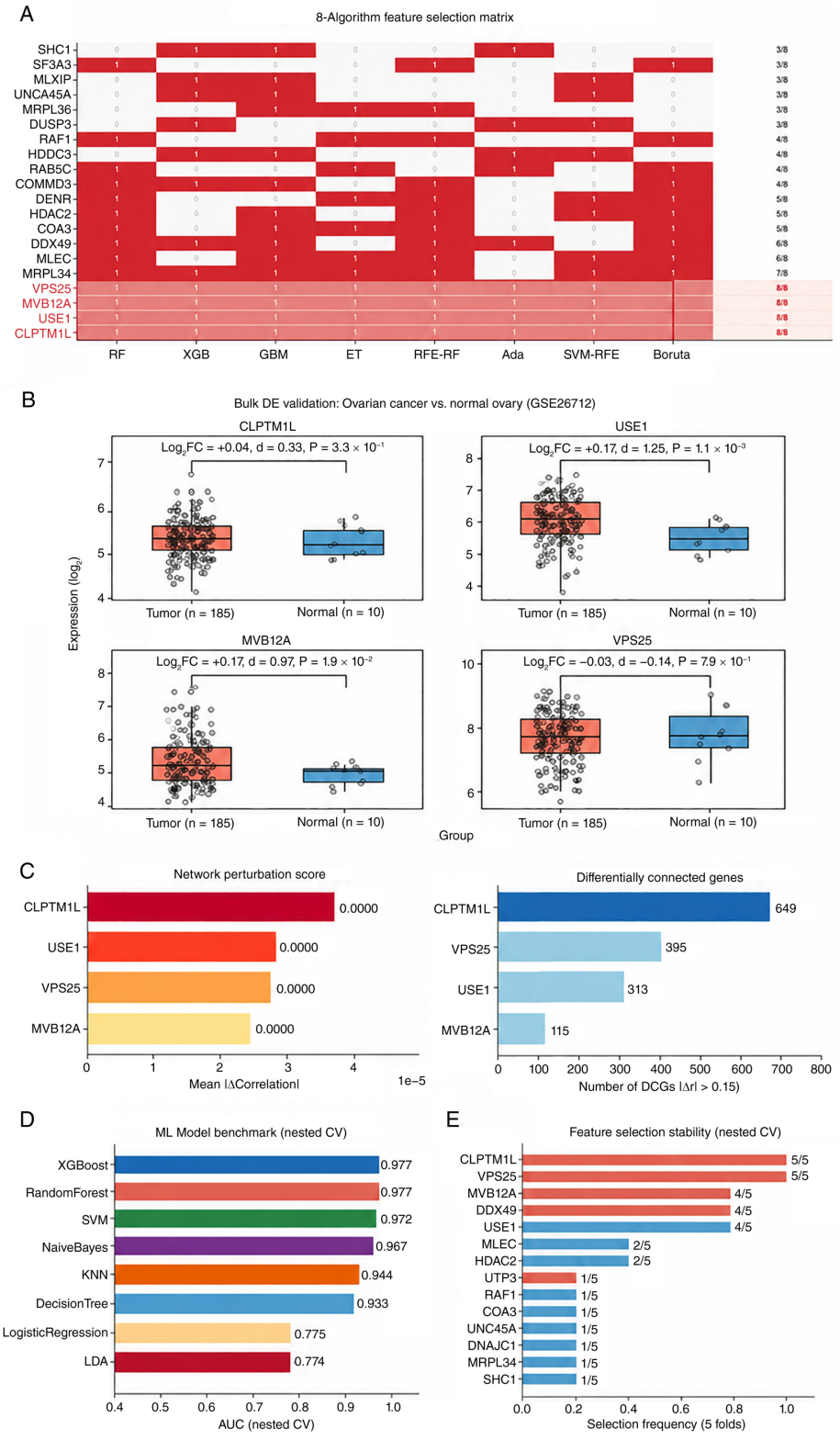


Figure 4. Integrated analysis prioritizes CLPTM1L and USE1 as key genes for functional validation. (A) Feature-selection matrix presenting genes retained by eight algorithms: RF, XGB, GBM, ET, RFE-RF, Ada, SVM-RFE and Boruta. CLPTM1L, USE1, MVB12A and VPS25 were retained by all eight algorithms. (B) External validation of the expression levels of the four candidate genes in the GSE26712 dataset by comparing OC with normal ovarian samples. The corresponding $\log_2$ FC and P-values are presented in each panel. (C) Virtual knockout summary showing the mean absolute change in gene-gene correlation and the number of DCGs for each candidate. DCGs were defined by $|\Delta r|>0.15$. (D) ROC-AUC performance of eight classifiers under nested cross-validation. (E) Feature-selection stability across the five outer folds of nested cross-validation. CLPTM1L, cleft lip and palate transmembrane protein 1-like; USE1, unconventional soluble N-ethylmaleimide-sensitive factor attachment protein receptor in the endoplasmic reticulum 1; MVB12A, multivesicular body subunit 12A; VPS25, vacuolar protein sorting 25 homolog; RF, random forest; XGB, extreme gradient boosting; GBM, gradient boosting machine; ET, extremely randomized trees; RFE-RF, recursive feature elimination with RF; Ada, adaptive boosting; SVM-RFE, support vector machine-RFE; OC, ovarian cancer; TWAS, transcriptome-wide association study; HTS, high-TWAS state; MTS, middle-TWAS state; LTS, low-TWAS state; ROC-AUC, receiver operating characteristic area under the curve; KNN, K-nearest neighbors; LDA, linear discriminant analysis; FC, fold change; DCG, differentially connected gene. DE, differential expression; ML, machine learning; CV, cross-validation.

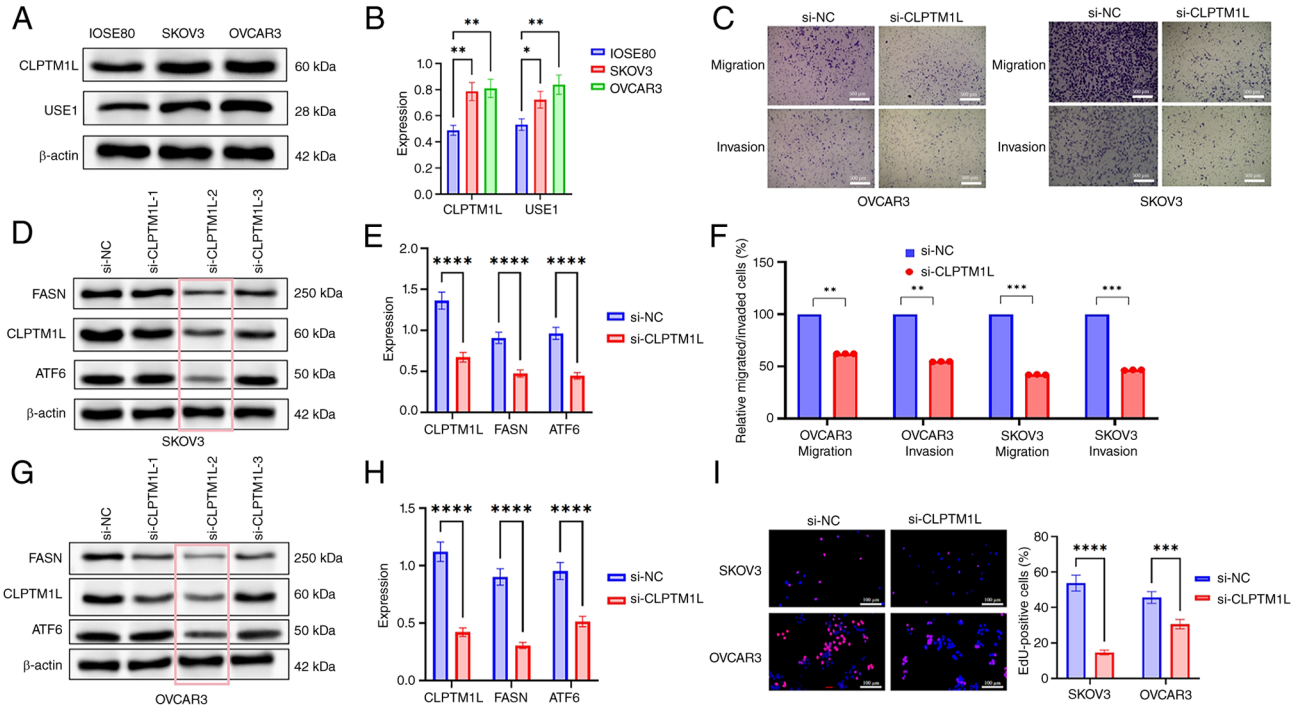


Figure 5. CLPTM1L knockdown inhibits ovarian cancer cell migration, invasion and DNA synthesis, and is accompanied by reduced FASN and ATF6 expression. (A) Baseline western blotting of CLPTM1L and USE1 in IOSE80, SKOV3 and OVCAR3 cells. (B) Densitometric semi-quantification of baseline CLPTM1L and USE1 protein expression. (C) Representative images from Transwell migration and Matrigel invasion assays of OVCAR3 and SKOV3 cells following CLPTM1L knockdown. (D) Western blotting after transfection of three CLPTM1L-targeting siRNAs in SKOV3 cells for the assessment of CLPTM1L, FASN and ATF6 expression. The red box indicates si-CLPTM1L-2, which was selected for subsequent experiments. (E) Densitometric semi-quantification of CLPTM1L, FASN and ATF6 expression following treatment with si-CLPTM1L-2 in SKOV3 cells. (F) Quantification of migration and invasion following CLPTM1L knockdown in OVCAR3 and SKOV3 cells. Values were normalized to those of the corresponding si-NC group. (G) Western blotting analysis of protein expression in OVCAR3 cells. The red box indicates the selected si-CLPTM1L-2. (H) Densitometric semi-quantification of CLPTM1L, FASN and ATF6 expression following treatment with si-CLPTM1L-2 in OVCAR3 cells. (I) Representative EdU staining images and quantification of EdU-positive cells following CLPTM1L knockdown. Data are presented as the mean ± SD from three independent experiments. For (B), CLPTM1L and USE1 expression levels were analyzed separately across IOSE80, SKOV3 and OVCAR3 cells using one-way ANOVA followed by Tukey's multiple comparisons test. For (E, F, H and I), comparisons between two independent groups were performed using unpaired two-tailed Student's t-tests. For (F), statistical testing was performed using the raw replicate cell counts prior to normalization. *P<0.05, **P<0.01, ***P<0.001 and ****P<0.0001. Scale bars, 500 μm in Transwell images and 100 μm in EdU images. CLPTM1L, cleft lip and palate transmembrane protein 1-like; FASN, fatty acid synthase; ATF6, activating transcription factor 6; USE1, unconventional soluble N-ethylmaleimide-sensitive factor attachment protein receptor in the endoplasmic reticulum 1; siRNA/si, small interfering RNA; NC, negative control; EdU, 5-ethynyl-2'-deoxyuridine.

ability to silence CLPTM1L and si-CLPTM1L-2 effectively reduced CLPTM1L expression in both SKOV3 and OVCAR3 cells (Fig. 5D, E, G and H). RT-qPCR further confirmed significant CLPTM1L knockdown in SKOV3 and OVCAR3 cells (Fig. S9A).

The effects of CLPTM1L knockdown on cell motility were evaluated using Transwell assays. Representative images indicated fewer migrating cells following CLPTM1L knockdown in both cell lines (Fig. 5C). Matrigel invasion assays similarly demonstrated reduced invasion. Quantitative analysis confirmed significant reductions in both migration and invasion compared with those in the corresponding si-NC groups (Fig. 5F).

DNA synthesis was assessed using EdU staining. The proportion of EdU-positive cells was reduced following CLPTM1L knockdown in both SKOV3 and OVCAR3 cells (Fig. 5I), indicating that CLPTM1L depletion impaired DNA synthesis.

Protein alterations associated with CLPTM1L knockdown were also evaluated. Western blotting demonstrated that FASN and ATF6 protein expression was decreased concomitantly with CLPTM1L expression in both OC cell lines (Fig. 5D, E, G and H). Thus, CLPTM1L knockdown inhibited migration, invasion and DNA synthesis, and was accompanied by reduced FASN and ATF6 protein expression.

USE1 knockdown inhibits OC cell migration, invasion and DNA synthesis, and is accompanied by reduced MFF and ATF6 expression. Baseline western blotting demonstrated higher USE1 protein expression in SKOV3 and OVCAR3 cells than in IOSE80 cells (Fig. 5A and B). Western blotting confirmed an effective reduction in USE1 protein expression following transfection with si-USE1-1 (Fig. 6A, B, D and E). RT-qPCR further confirmed significant USE1 knockdown in SKOV3 and OVCAR3 cells (Fig. S9B).

Transwell assays indicated that USE1 knockdown reduced the migration of both SKOV3 and OVCAR3 cells (Fig. 6C and F). Matrigel invasion was also reduced following USE1 silencing. Quantitative analysis confirmed significant inhibition of both migration and invasion compared with those in the si-NC groups.

EdU staining revealed fewer EdU-positive cells following USE1 knockdown (Fig. 6G and H), indicating that USE1 depletion impaired DNA synthesis in both OC cell lines.

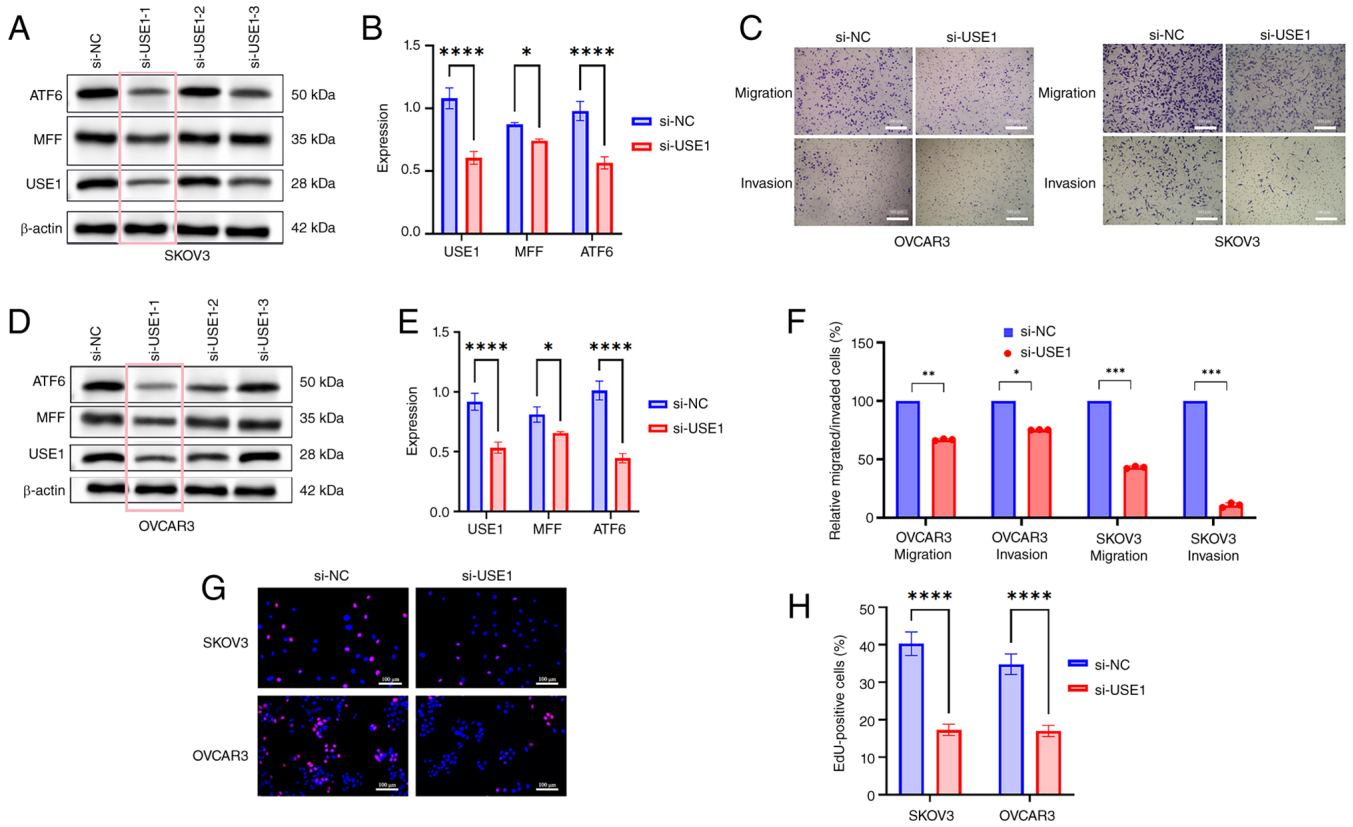


Figure 6. USE1 knockdown inhibits ovarian cancer cell migration, invasion and DNA synthesis, and is accompanied by reduced MFF and ATF6 expression. (A) Western blotting following transfection of three USE1-targeting siRNAs in SKOV3 cells for the assessment of USE1, MFF and ATF6 expression. The red box indicates si-USE1-1, which was selected for subsequent experiments. (B) Densitometric semi-quantification of USE1, MFF and ATF6 expression following treatment with si-USE1-1 in SKOV3 cells. (C) Representative images from Transwell migration and Matrigel invasion assays of OVCAR3 and SKOV3 cells following USE1 knockdown. (D) Western blotting for USE1, MFF and ATF6 in OVCAR3 cells transfected with three USE1-targeting siRNAs. The red box indicates si-USE1-1, which was selected for subsequent experiments. (E) Densitometric semi-quantification of USE1, MFF and ATF6 expression in OVCAR3 cells. (F) Quantification of migration and invasion following USE1 knockdown in OVCAR3 and SKOV3 cells. Values were normalized to those of the corresponding si-NC group. (G) Representative EdU staining images following USE1 knockdown in SKOV3 and OVCAR3 cells. (H) Quantification of EdU-positive cells. Data are presented as the mean ± SD from three independent experiments. Comparisons between two independent groups in (B, E, F and H) were performed using unpaired two-tailed Student's t-tests. For (F), statistical testing was performed using the raw replicate cell counts prior to normalization. *P<0.05, **P<0.01, ***P<0.001 and ****P<0.0001. Scale bars, 500 μm in Transwell images and 100 μm in EdU images. USE1, unconventional soluble N-ethylmaleimide-sensitive factor attachment protein receptor in the endoplasmic reticulum 1; MFF, mitochondrial fission factor; ATF6, activating transcription factor 6; siRNA/si, small interfering RNA; NC, negative control; EdU, 5-ethynyl-2'-deoxyuridine.

Western blotting was performed to assess MFF and ATF6 expression. The expression levels of both proteins were reduced following USE1 knockdown in SKOV3 and OVCAR3 cells (Fig. 6A, B, D and E). These results demonstrated that USE1 knockdown inhibited migration, invasion and DNA synthesis, and was accompanied by reduced MFF and ATF6 protein expression.

Discussion

The present study integrated genetic susceptibility analyses with single-cell transcriptomics and cell-based experiments to investigate HGSOC at multiple biological levels. The genetically prioritized gene set exhibited heterogeneous activity across epithelial cells and was used to define HTS, MTS and LTS. These states differed in their transcriptional programs and inferred cell-cell communication patterns. Subsequent feature-selection analyses retained four candidate genes, of which CLPTM1L and USE1 were selected for experimental evaluation. Knockdown of either gene significantly reduced migration, invasion and DNA synthesis in SKOV3 and OVCAR3 cells. These findings extended the associations of CLPTM1L and USE1 with genetic susceptibility and epithelial-state activity to measurable changes in OC cell behavior.

The epithelial state analysis provided cellular context for the genetic susceptibility data. Although TWAS and eQTL analyses can prioritize genes associated with inherited risk, they do not reveal how these genes are distributed across heterogeneous tumor cell populations. HGSOC is characterized by transcriptionally diverse tumor cell populations (24,25). Longitudinal and single-cell studies have identified recurrent programs related to proliferation, metabolism, stress responses, DNA repair and chemoresistance, whose relative abundance changes during disease progression and treatment (2,26,27). Chromatin and spatial analyses have also characterized treatment-associated residual tumor states and metastatic programs (28,29). Furthermore, single-cell and spatial studies have demonstrated that OC cells interact with distinct immune and stromal microenvironments in

primary tumors, metastatic sites and ascites, and after chemotherapy (30-33). In the present study, HTS, MTS and LTS formed a continuous activity gradient rather than discrete cell lineages. Nevertheless, HTS and LTS cells differed in pathway activity, with higher mean activity across the representative pathways in LTS cells, and the communication analysis showed pathway-specific cancer-associated changes. These findings suggested that genes prioritized on the basis of inherited susceptibility were unevenly distributed across epithelial states. Therefore, the state labels should be interpreted as relative activity groups within the epithelial compartment rather than fixed biological subtypes.

Four genes, CLPTM1L, USE1, MVB12A and VPS25, were retained by the feature-selection analyses. MVB12A received particularly strong support from both the genetic analysis and ovary eQTL data, whereas VPS25 was also consistently retained during candidate selection. As neither gene was evaluated experimentally in the present study, their functional roles cannot be inferred from the computational findings alone. CLPTM1L and USE1 were selected for further investigation because they were supported by genetic prioritization, epithelial-state analysis, feature selection, external expression analysis and virtual knockout analysis and were selected as two representative candidates for experimental validation; MVB12A and VPS25 were not excluded from cellular validation. Some experimental evidence regarding CLPTM1L in OC is already available. Parashar *et al* (34) reported elevated CLPTM1L expression in ovarian tumor cells and demonstrated that CLPTM1L inhibition could increase sensitivity to platinum-based treatment. The present study examined a different aspect of CLPTM1L function. CLPTM1L knockdown significantly reduced migration, invasion and DNA synthesis in two OC cell lines. USE1 has been less extensively studied in OC. USE1 is a component of the endoplasmic reticulum-associated soluble N-ethylmaleimide-sensitive factor attachment protein receptor machinery involved in membrane trafficking (35); however, its role in OC cells remains poorly defined. In the present study, USE1 knockdown produced effects similar to those observed following CLPTM1L depletion; significantly reducing migration, invasion and EdU incorporation. These findings suggested functional roles for both genes in the cellular phenotypes examined, although the underlying mechanisms remain to be determined.

The alterations in FASN, MFF and ATF6 expression provide preliminary molecular clues but should be interpreted separately from the functional assay results. CLPTM1L knockdown was accompanied by a significant reduction in FASN and ATF6 protein expression, whereas USE1 knockdown was accompanied by a significant reduction in MFF and ATF6 expression. FASN serves an established role in lipid synthesis, and pharmacological or genetic interference with FASN has been investigated in OC cells (36). MFF regulates mitochondrial fission, and previous work in OC has demonstrated that MFF expression and mitochondrial dynamics can influence tumor cell proliferation and tumor progression (37). ATF6 is a component of the endoplasmic reticulum stress response, and increased ATF6 signaling has been associated with resistance to poly ADP-ribose polymerase inhibitors in OC models (38). These previous findings support the biological relevance of the observed protein alterations but do not establish the relationships of FASN, MFF or ATF6 with CLPTM1L or USE1 in the present study. Direct regulation, protein interactions, functional rescue experiments using FASN, MFF or ATF6, and pathway-specific inhibition were not examined. Therefore, the present study demonstrated associated molecular alterations rather than established CLPTM1L-FASN-ATF6 or USE1-MFF-ATF6 pathways.

Virtual knockout analysis provided an additional means of evaluating candidate genes within the epithelial cell network. Virtual knockout of CLPTM1L and USE1 altered network connectivity, with virtual knockout of CLPTM1L producing the strongest perturbation among the four candidates. A previous single-cell study similarly used gene regulatory network inference to prioritize candidate features in HGSOC (39). In the present study, virtual knockout analysis supported the selection of CLPTM1L and USE1 for experimental evaluation but could not substitute for gene perturbation in cells. The same limitation applies to the machine learning analysis. Its purpose was to narrow the candidate set and identify genes consistently retained by different selection methods, rather than to establish a clinical classifier. Therefore, the *in vitro* investigations served to determine whether candidates selected through computational analyses also influenced cellular phenotypes.

Several limitations should be acknowledged. First, the epithelial state analysis was based on public single-cell datasets. Although the activity groups were resolved in the current analysis, their reproducibility should be evaluated in additional HGSOC cohorts. Second, the functional experiments were conducted in SKOV3 and OVCAR3 cells. Additional OC models, particularly those with well-defined molecular characteristics of HGSOC, would strengthen the biological interpretation of the findings. IOSE80 cells were used only as a non-malignant baseline comparator and were not subjected to functional knockdown experiments; therefore, whether CLPTM1L or USE1 silencing produces similar phenotypes in non-malignant ovarian epithelial cells remains unknown. Third, the experiments relied primarily on siRNA-mediated knockdown. The absence of overexpression and rescue experiments limits the causal interpretation of the observed phenotypes. Fourth, alterations in FASN, MFF and ATF6 were assessed only at the level of protein expression. Their relationships with CLPTM1L and USE1 require further experimental investigation. Finally, virtual knockout and cell-cell communication analyses are computational approximations and should be regarded as supportive evidence rather than direct experimental validation.

Overall, these findings link genetically prioritized genes to epithelial state heterogeneity and functional phenotypes in OC cells. Knockdown of either CLPTM1L or USE1 reduced migration, invasion and DNA synthesis in SKOV3 and OVCAR3 cells. The associated alterations in FASN, MFF and ATF6 suggested potential directions for further investigation. However, the current evidence does not define the underlying regulatory pathways.

Acknowledgements

Not applicable.

Funding

The present work was supported by the Chongqing Graduate Student Research Innovation Project, Chongqing Municipal Education Commission (grant no. CYS25368).

Availability of data and materials

The data generated in the present study may be requested from the corresponding author.

Authors' contributions

ZH, LQ and LL conceived and designed the study. ZH, HT, WK, LQ and LL developed the methodology. ZH and HT performed the bioinformatics analyses. WK, WS and YL performed the experimental validation. ZH, HT and WS performed formal analysis. WK, WS, YL and WH performed the investigations. GW, LQ and LL provided resources. GW additionally contributed to the interpretation of the experimental results and critically revised the manuscript for important intellectual content. ZH, HT and YL curated the data. ZH and HT wrote the original draft. GW, LQ and LL reviewed and edited the manuscript. ZH, HT and WS prepared the figures. LQ and LL supervised the study and were responsible for project administration. ZH and HT confirm the authenticity of all the raw data. All authors have read and approved the final version of the manuscript.

Ethics approval and consent to participate

Not applicable.

Patient consent for publication

Not applicable.

Competing interests

The authors declare that they have no competing interests.

References

1. Zhang K, Erkan EP, Jamalzadeh S, Dai J, Andersson N, Kaipio K, Lamminen T, Mansuri N, Huhtinen K, Carpén O, *et al*: Longitudinal single-cell RNA-seq analysis reveals stress-promoted chemoresistance in metastatic ovarian cancer. Sci Adv 8: eabm1831, 2022.
2. Nath A, Cosgrove PA, Mirsafian H, Christie EL, Pflieger L, Copeland B, Majumdar S, Cristea MC, Han ES, Lee SJ, *et al*: Evolution of core archetypal phenotypes in progressive high grade serous ovarian cancer. Nat Commun 12: 3039, 2021.
3. Bray F, Laversanne M, Sung H, Ferlay J, Siegel RL, Soerjomataram I and Jemal A: Global cancer statistics 2022: GLOBOCAN estimates of incidence and mortality worldwide for 36 cancers in 185 countries. CA Cancer J Clin 74: 229-263, 2024.
4. Labidi-Galy SI, Papp E, Hallberg D, Niknafs N, Adleff V, Noe M, Bhattacharya R, Novak M, Jones S, Phallen J, *et al*: High grade serous ovarian carcinomas originate in the fallopian tube. Nat Commun 8: 1093, 2017.
5. Izar B, Tirosh I, Stover EH, Wakiro I, Cuoco MS, Alter I, Rodman C, Leeson R, Su MJ, Shah P, *et al*: A single-cell landscape of high-grade serous ovarian cancer. Nat Med 26: 1271-1279, 2020.
6. Xu J, Fang Y, Chen K, Li S, Tang S, Ren Y, Cen Y, Fei W, Zhang B, Shen Y and Lu W: Single-cell RNA sequencing reveals the tissue architecture in human high-grade serous ovarian cancer. Clin Cancer Res 28: 3590-3602, 2022.
7. Wang Y, Xie H, Chang X, Hu W, Li M, Li Y, Liu H, Cheng H, Wang S, Zhou L, *et al*: Single-cell dissection of the multiomic landscape of high-grade serous ovarian cancer. Cancer Res 82: 3903-3916, 2022.
8. Barnes DR, Tyrer JP, Dennis J, Leslie G, Bolla MK, Lush M, Aeilts AM, Aittomäki K, Andrieu N, Andrulis IL, *et al*: Genome-wide association study of 398,238 women unveils seven loci associated with high-grade serous ovarian cancer. NPJ Genom Med 10: 73, 2025.
9. Dareng EO, Coetzee SG, Tyrer JP, Peng PC, Rosenow W, Chen S, Davis BD, Dezem FS, Seo JH, Nameki R, *et al*: Integrative multi-omics analyses to identify the genetic and functional mechanisms underlying ovarian cancer risk regions. Am J Hum Genet 111: 1061-1083, 2024.
10. Lu Y, Beeghly-Fadiel A, Wu L, Guo X, Li B, Schildkraut JM, Im HK, Chen YA, Permuth JB, Reid BM, *et al*: A transcriptome-wide association study among 97,898 women to identify candidate susceptibility genes for epithelial ovarian cancer risk. Cancer Res 78: 5419-5430, 2018.
11. Gusev A, Lawrenson K, Lin X, Lyra PC, Kar S, Vavra KC, Segato F, Fonseca MAS, Lee JM, Pejovic T, *et al*: A transcriptome-wide association study of high-grade serous epithelial ovarian cancer identifies new susceptibility genes and splice variants. Nat Genet 51: 815-823, 2019.
12. Head ST, Dezem F, Todor A, Yang J, Plummer J, Gayther S, Kar S, Schildkraut J and Epstein MP: Cis- and trans-eQTL TWASs of breast and ovarian cancer identify more than 100 susceptibility genes in the BCAC and OCAC consortia. Am J Hum Genet 111: 1084-1099, 2024.
13. Dinh HQ, Lin X, Abbasi F, Nameki R, Haro M, Olingy CE, Chang H, Hernandez L, Gayther SA, Wright KN, *et al*: Single-cell transcriptomics identifies gene expression networks driving differentiation and tumorigenesis in the human fallopian tube. Cell Rep 35: 108978, 2021.
14. Han X, Gao Y, Jiang M, Li Z, Guo J, Li Y, Yi J, Hou L, Cheng J, Feng L, *et al*: Single-cell and spatial transcriptome sequencing uncover a platinum-resistant cluster overexpressed TACSTD2 in high-grade serous ovarian cancer. J Cancer 15: 3427-3440, 2024.
15. Carvalho RF, do Canto LM, Abildgaard C, Aagaard MM, Tronhjem MS, Waldstrøm M, Jensen LH, Steffensen KD and Rogatto SR Single-cell and bulk RNA sequencing reveal ligands and receptors associated with worse overall survival in serous ovarian cancer. Cell Commun Signal 20: 176, 2022.
16. Ferri-Borgogno S, Zhu Y, Sheng J, Burks JK, Gomez JA, Wong KK, Wong STC and Mok SC: Spatial transcriptomics depict ligand-receptor cross-talk heterogeneity at the tumor-stroma interface in long-term ovarian cancer survivors. Cancer Res 83: 1503-1516, 2023.
17. GTEx Consortium: The GTEx Consortium atlas of genetic regulatory effects across human tissues. Science 369: 1318-1330, 2020.
18. Bonome T, Levine DA, Shih J, Randonovich M, Pise-Masison CA, Bogomolniy F, Ozbun L, Brady J, Barrett JC, Boyd J and Birrer MJ: A gene signature predicting for survival in suboptimally debulked patients with ovarian cancer. Cancer Res 68: 5478-5486, 2008.
19. Koti M, Gooding RJ, Nuin P, Haslehurst A, Crane C, Weberpals J, Childs T, Bryson P, Dharsee M, Evans K, *et al*: Identification of the IGF1/PI3K/NF κB/ERK gene signalling networks associated with chemotherapy resistance and treatment response in high-grade serous epithelial ovarian cancer. BMC Cancer 13: 549, 2013.
20. Tothill RW, Tinker AV, George J, Brown R, Fox SB, Lade S, Johnson DS, Trivett MK, Etemadmoghadam D, Locandro B, *et al*: Novel molecular subtypes of serous and endometrioid ovarian cancer linked to clinical outcome. Clin Cancer Res 14: 5198-5208, 2008.
21. Lisowska KM, Olbryt M, Dudaladava V, Pamula-Pilat J, Kujawa K, Grzybowska E, Jarząb M, Student S, Rzepecka IK, Jarząb B, *et al*: Gene expression analysis in ovarian cancer-faults and hints from DNA microarray study. Front Oncol 4: 6, 2014.
22. Cancer Genome Atlas Research Network: Integrated genomic analyses of ovarian carcinoma. Nature 474: 609-615, 2011.
23. Livak KJ and Schmittgen TD: Analysis of relative gene expression data using real-time quantitative PCR and the 2(-Delta Delta C(T)) method. Methods 25: 402-408, 2001.

24. Zhao F, Jiang X, Li Y, Huang T, Xiahou Z, Nie W and Li Q: Characterizing tumor biology and immune microenvironment in high-grade serous ovarian cancer via single-cell RNA sequencing: Insights for targeted and personalized immunotherapy strategies. Front Immunol 15: 1500153, 2025.
25. Gao C, Lv X, Pan A, Chen L, Liu Q, Zhang D and Wu W: Single-cell transcriptomic analysis reveals intra-tumoral heterogeneity and immunotherapy strategies in high-grade serous ovarian cancer. iScience 29: 115266, 2026.
26. Wang Y, Tang Z, Li H, Zhou R, Wu H, Cen X, Zhang Y, Dong W and Yang H: Chemoresistance evolution in ovarian cancer delineated by single-cell RNA sequencing. Int J Mol Sci 26: 6760, 2025.
27. Li Z, Li J, Li Y, Yi J, Zhao X and Yue W: Single-cell transcriptomics identify a chemotherapy-resistance related cluster overexpressed CLIC3 in ovarian cancer. Discov Oncol 16: 1099, 2025.
28. Croft W, Pounds R, Jeevan D, Singh K, Balega J, Sundar S, Williams A, Ganesan R, Kehoe S, Ott S, *et al*: The chromatin landscape of high-grade serous ovarian cancer metastasis identifies regulatory drivers in post-chemotherapy residual tumour cells. Commun Biol 7: 1211, 2024.
29. Qin LH, Jiang Z, Yang C, Song R, Chen PY, Xu W, Zeng G, Liao JY and Long L: Spatial single-cell maps reveal ST6GAL1 promoting ovarian cancer metastasis. Glycoconj J 42: 27-40, 2025.
30. Zheng X, Wang X, Cheng X, Liu Z, Yin Y, Li X, Huang Z, Wang Z, Guo W, Ginhoux F, *et al*: Single-cell analyses implicate ascites in remodeling the ecosystems of primary and metastatic tumors in ovarian cancer. Nat Cancer 4: 1138-1156, 2023.
31. Hu X, Du C, Du D, Zhang Y, Gao H and Tao M: Single cell transcriptomic analysis reveals molecular mechanisms of chemoresistance and immune microenvironment remodeling in ovarian cancer. Discov Oncol 16: 2118, 2025.
32. Launonen IM, Niemiec I, Hincapie-Otero M, Erkan EP, Junquera A, Afenteva D, Falco MM, Liang Z, Salko M, Chamchougia F, *et al*: Chemotherapy induces myeloid-driven spatially confined T cell exhaustion in ovarian cancer. Cancer Cell 42: 2045-2063.e10, 2024.
33. Perez-Villatoro F, Shabanova A, van Wagensveld L, Junquera A, Niemiec I, Hincapie-Otero MM, Kang Z, Falco MM, Birgin K, Wolf S, *et al*: Single-cell spatial atlas of high-grade serous ovarian cancer uncovers MHC class II as a key predictor of spatial tumor ecosystems and clinical outcomes. Cancer Discov 16: 1100-1125, 2026.
34. Parashar D, Geethadevi A, McAllister D, Ebben J, Peterson FC, Jensen DR, Bishop E, Pradeep S, Volkman BF, Dwinell MB, *et al*: Targeted biologic inhibition of both tumor cell-intrinsic and intercellular CLPTM1L/CRR9-mediated chemotherapeutic drug resistance. NPJ Precis Oncol 5: 16, 2021.
35. Aoki T, Kojima M, Tani K and Tagaya M: Sec22b-dependent assembly of endoplasmic reticulum Q-SNARE proteins. Biochem J 410: 93-100, 2008.
36. Grunt TW, Slany A, Semkova M, Colomer R, Lopez-Rodriguez ML, Wuczkowski M, Wagner R, Gerner C and Stübiger G: Membrane disruption, but not metabolic rewiring, is the key mechanism of anticancer-action of FASN-inhibitors: A multi-omics analysis in ovarian cancer. Sci Rep 10: 14877, 2020.
37. Zhu Y, Wang Y, Li Y, Li Z, Kong W, Zhao X, Chen S, Yan L, Wang L, Tong Y and Shao H: Carnitine palmitoyltransferase 1A promotes mitochondrial fission by enhancing MFF succinylation in ovarian cancer. Commun Biol 6: 618, 2023.
38. McMellen A, Yamamoto TM, Qamar L, Sanders BE, Nguyen LL, Ortiz Chavez D, Bapat J, Berning A, Post MD, Johnson J, *et al*: ATF6-mediated signaling contributes to PARP inhibitor resistance in ovarian cancer. Mol Cancer Res 21: 3-13, 2023.
39. Itai T, Dai Y, Liu W, Lee DF and Zhao Z: Investigating prognostic features in high-grade serous ovarian cancer through gene regulatory network inference with single-cell transcriptomic profiles. Sci Rep 15: 39345, 2025.

Copyright © 2026 He et al. This work is licensed under a Creative Commons Attribution 4.0 International (CC BY 4.0) License.